geosciences

Article

The Afghanistan Earthquake of 21 June 2022: The Role of Compressional Step-Overs in Seismogenesis

Tejpal Singh [1,*], Nardeep Nain [1,2], Fernando Monterroso [3], Riccardo Caputo [4,*], Pasquale Striano [3], R. B. S. Yadav [2], Chittenipattu Puthenveettil Rajendran [5], Anil G. Sonkusare [1], Claudio De Luca [3] and Riccardo Lanari [3]

[1] CSIR-Central Scientific Instruments Organisation, Chandigarh 160030, India; nrdeepnn@gmail.com (N.N.); anilsonkusare@csio.res.in (A.G.S.)
[2] Department of Geophysics, Kurukshetra University, Kurukshetra 136119, India; rbskuk@gmail.com
[3] CNR-IREA (Istituto per il Rilevamento Elettromagnetico dell'Ambiente), 80124 Naples, Italy; monterroso.f@irea.cnr.it (F.M.); striano.p@irea.cnr.it (P.S.); deluca.c@irea.cnr.it (C.D.L.); lanari.r@irea.it (R.L.)
[4] Department of Physics and Earth Sciences, University of Ferrara, 44122 Ferrara, Italy
[5] National Institute of Advanced Studies, Bengaluru 560012, India; cprajendran@gmail.com
* Correspondence: tejpal@csio.res.in (T.S.); rcaputo@unife.it (R.C.)

Abstract: The Afghanistan earthquake of 21 June 2022 ruptured a ~10 km-long fault segment in the North Waziristan–Bannu fault system (NWBFS) located towards the north of the Katawaz Basin. The earthquake was shallow and reportedly caused widespread devastation. In this article, we investigated the long-term, i.e., geological and geomorphological, evidence of deformation along the earthquake segment. For comparison, we also studied the short-term space geodetic and remote sensing results documenting a visible offset between the fault traces. Focusing on the fault modelling and on the published results, it is thus clear that the earthquake rupture did not reach the surface; instead, it stopped in the shallow sub-surface at ~1 km depth. Moreover, the InSAR analyses show some technical issues, such as coherence loss, etc., likely due to severe ground-shaking leaving some gaps in the results; geological and geomorphological evidence complemented this information. As an outcome of this research, we confirmed that InSAR results could generally capture the overall fault geometry at depth, even in cases of blind faulting, whereas the detailed geometry of the tectonic structure, in this case with a right stepping en-echelon pattern, could be successfully captured by combining it with geological and geomorphological approaches and optical remote sensing observations. Accordingly, the right stepping fault generates a restraining bend in the dominantly left-lateral shear zone. Therefore, such fault stepovers are capable of localizing strain and could act as loci for seismic ruptures, bearing strong implications for the seismic hazard assessment of the region, as well as of other strike-slip fault zones.

Keywords: morphotectonics; SAR interferometry; seismotectonics; fault model; satellite analyses

Academic Editor: Cristina Totaro

Received: 1 February 2025
Revised: 28 March 2025
Accepted: 31 March 2025
Published: 18 April 2025

Citation: Singh, T.; Nain, N.; Monterroso, F.; Caputo, R.; Striano, P.; Yadav, R.B.S.; Rajendran, C.P.; Sonkusare, A.G.; De Luca, C.; Lanari, R. The Afghanistan Earthquake of 21 June 2022: The Role of Compressional Step-Overs in Seismogenesis. *Geosciences* **2025**, *15*, 156. https://doi.org/10.3390/geosciences15040156

1. Introduction

The India–Eurasia collision and subsequent convergence since the last ~55 Ma has produced spectacular topography all along the plate margin (Figure 1). In the north, it is primarily dominated by the thrusting and uplift of the Himalayan mountain belt, whereas along the western and eastern plate boundaries, it is controlled by strike-slip faulting along the Chaman fault (CF) and Sagaing fault (SF), respectively (Figure 1). The tectonic boundary all along is characterized by frequent seismicity, causing loss of life and property, which is a matter of concern to society and the scientific community. As a scientific contribution, we present an assessment on the nature of faulting, surface topography and its relationship to the damage caused by the earthquake. In this particular study, the focus is on the western boundary, along which an earthquake occurred on 21 June 2022 in eastern Afghanistan, close to the border with Pakistan (Figure 2). The earthquake area is located in a difficult terrain with poor access from either bordering country, where the surface deformation and the reported damage warranted assessment. Remote sensing techniques play a crucial role in overcoming the limitations of field accessibility, and thereby form the motivation of this study. Accordingly, InSAR measurements and optical remote sensing observations combined with the geological and geomorphic background have been used to elaborate on the co-seismic surface manifestation to constrain the sub-surface geometry of the causative fault segment.

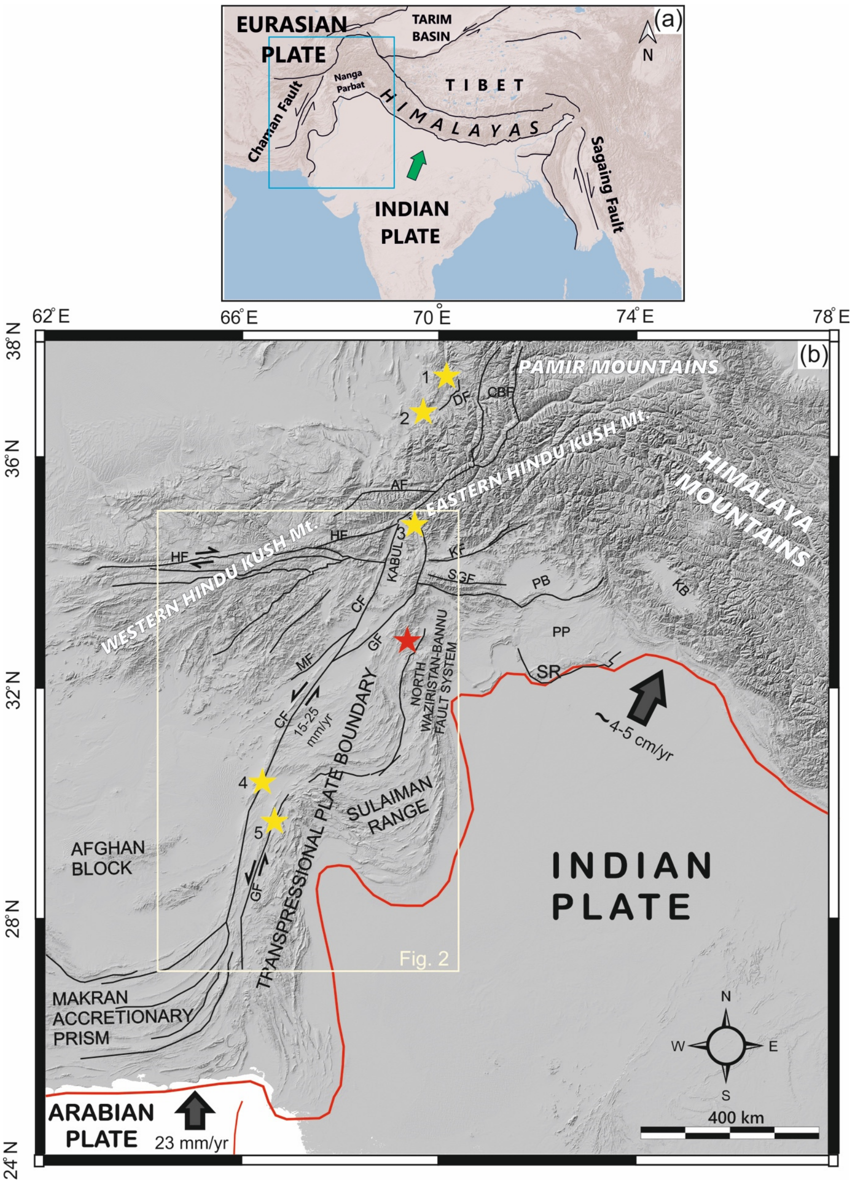

Figure 1. The India–Asia convergence zone (**a**) showing the major thrusts towards the north generating the Himalayan mountain belt and the western and eastern boundary showing the major strike-slip faulting along the Chaman fault (CF) and Sagaing fault (SF), respectively. (**b**) The western

plate boundary defined by the localized deformation along the Chaman fault (CF) and a series of subsidiary faults trending parallel to sub-parallel to it spread out over a wide lithospheric shear zone forming the Chaman Transpressional Zone (CTZ). The red line marks the plate boundary. The bold arrows show the general direction of plate motion alongwith approximate rates. The yellow stars show major historical earthquakes along the CTZ, and the red star shows the 21 June 2022 event. Other important features in the figure include PB: Peshawar basin; PP: Potwar plateau; SR: salt range; SGF: Spinghar fault; HF: Herat fault; GF: Gardez fault; MF: Mokur fault; KF: Konar fault; AF: Andrab fault; CBF: Central Badakhshan fault; KB: Kashmir basin.

With this premise, we investigated the meizoseismal area of the 21 June 2022 Afghanistan earthquake. The causative fault appears to be a part of the broader North Waziristan Bannu fault system (NWBFS), which extends E-W for more than 100 km (Figure 1), belonging to the much wider Sulaiman Range. The Sulaiman Range is tectonically active region with a complex fault geometry following the lobate surface pattern of the range [1,2]. The present investigation will allow to better understand the correlation between long-term deformation signatures in the geology and geomorphology of the area with the short-term remote sensing observations and InSAR measurements along the recently activated fault segment that was responsible for the 21 June 2022 event.

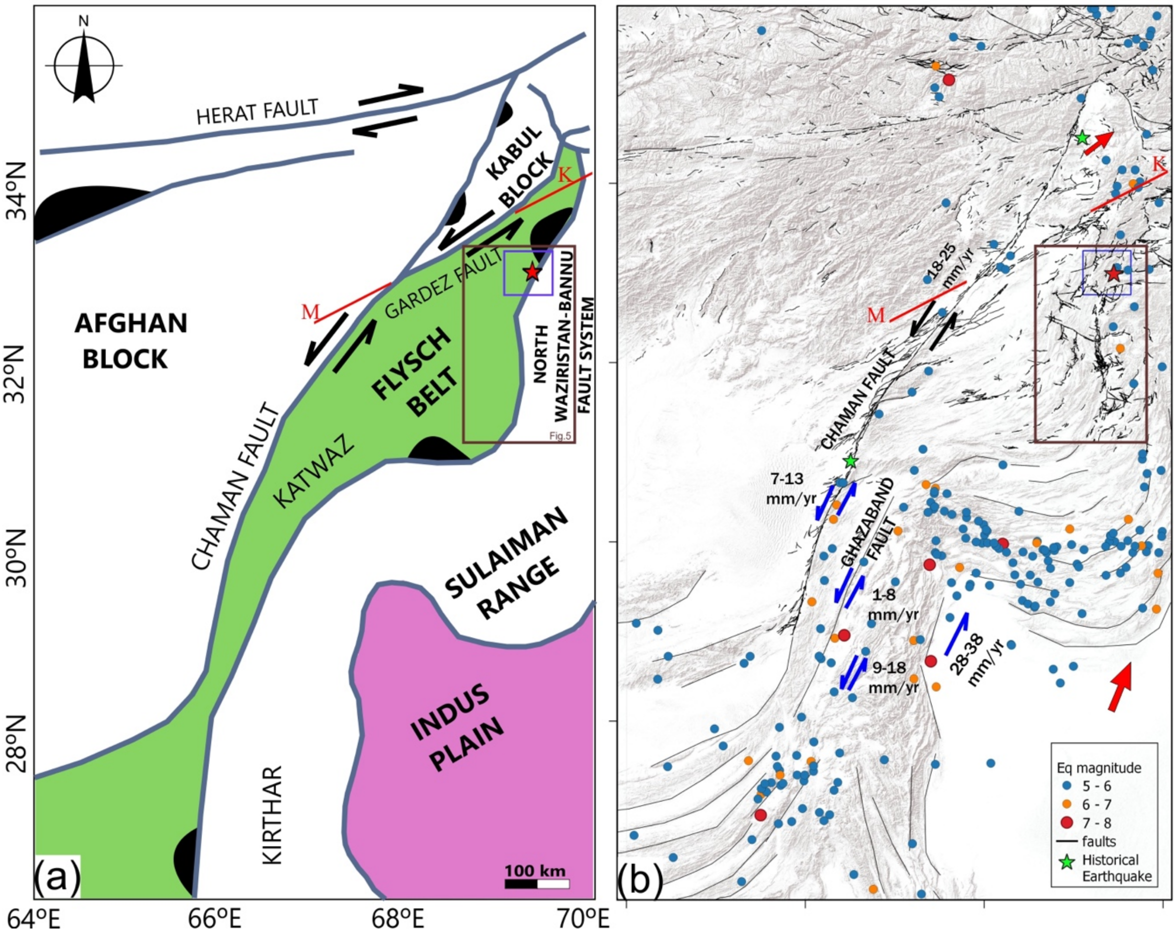

Figure 2. (**a**) Tectonic divisions of the Western Plate boundary showing major faults by bold lines and subsidiary structures by normal lines. (**b**) Active faults from Ruleman et al. [3] and seismicity > 5 (USGS), bold arrows show the tectonic transport direction. M: Mokur fault and K: Konar fault. Black filled spaces represent ophiolites. Arrows show relative tectonic motions.

The major goals of the present study include the following: (i) mapping the possible cumulative morphotectonic evidence of the reactivated fault segment and its lateral continuity, (ii) studying of the InSAR co-seismic deformation pattern of the 21 June 2022 event, (iii) modelling the best-fit fault geometry by inverting the InSAR measurements, and (iv) comparing between the long-term and short-term deformation features for obtaining a reasonable fault geometry and its role in seismogenesis.

2. Tectonic Setting

The 21 June 2022 earthquake was located close to the western plate boundary of the India–Asia convergence [4,5], where the northward-indenting Indian subcontinent moves past the Helmand Block of the Eurasian Plate [6,7]. As typical in oblique plate convergence settings, deformation is kinematically partitioned [8–10]. Indeed, transcurrency largely occurs along a major lithospheric-scale shear zone referred to as the Chaman fault system (CFS), while the contractional component perpendicular to the boundary is broadly accommodated within the flysch belt and the Sulaiman Range (Figure 2). The CFS is a ~1000 km-long, roughly N–S-oriented tectonic boundary that extends from the Hindu Kush mountains in northern Afghanistan to the Makran coast in southern Pakistan (e.g., [11]; Figure 1). Szeliga et al. [12] noticed that the current strain rate is further partitioned across the CFS, including the Gazaband and Chaman faults. Consequently, seismicity is relatively distributed, and few earthquakes have been recorded along the Chaman fault in historical times [13]. This suggests aseismic slip and/or distributed deformation across numerous other structures.

On the other hand, diffuse shortening affects the thick foredeep succession of the Tertiary Katawaz Basin, forming the so-called flysch belt, as well as the sedimentary succession developed along the Mesozoic Indian passive margin. The latter has been largely inverted and mainly detached on top of the underlying transitional-to-oceanic Indian crust, thus forming the present-day Sulaiman Range. Overall, they comprise an active transpressional deformational zone affecting this wide inter-plate setting (Figure 1). Indeed, the whole system accommodates the ~4–5 cm/yr convergence rate between the Indian and Eurasian plates [14–16]. The current displacement is partitioned across the plate boundary and results in seismic events and active widening of the plate boundary [17].

Although the CFS is a relatively sharp geological boundary, there are several synthetic fault splays running sub-parallel to the main structure such as the Gardez fault (GF), the Mokur fault (MF), the Konar fault (KF), etc., [18–21], forming a broad zone of active deformation. At the boundary between the flysch belt and the Sulaiman Range is the North Waziristan Bannu fault system (NWBFS) (Figure 2). More precisely, the earthquake of 21 June 2022 occurred on this fault system a few kilometres from the eastern border of Afghanistan, where the deposits of the Katawaz flysch belt (KFB) are in tectonic contact with the Kurram group belonging to the south Waziristan accretionary wedge (Figure 2).

3. Data and Methods

As mentioned above, one of the major objectives of the present study is to investigate the long-term and short-term deformation signatures of the new fault segment that caused the earthquake of 21 June 2022 earthquake affecting the region between eastern Afghanistan and western Pakistan. To achieve this objective, published historical and geological maps from various sources and at different scales have been used, together with the database of active faults of Afghanistan [3] and other available works [20,21]. The datasets were digitized and stored in a GIS for spatial correlation and analyses. Surface topography data were accessed through the United States Geological Survey portal and were used to generate shaded relief maps in different perspective directions to highlight topographic features in the attempt of correlating them to known tectonic features. Multi-resolution satellite imageries from Indian remote sensing (IRS) satellites and the LANDSAT constellation were used to compare the observations and inferences represented on geological maps and surface topography. These methods allowed elaborating on the activated fault segment using typical methods of tectonic geomorphology and spatial analyses using satellite remote sensing and digital elevation datasets. Our interpretation of possible recent faulting is based on the characteristic features such as presence of prominent and continuous escarpments, strong lineaments in bedrock, linear valleys and typical drainage patterns [22–24]. The data showed good spatial correlation between geologic and geomorphologic features and a comparison with mapped active faults.

In order to investigate the ground displacement associated with the 21 June 2022 event, we exploited the DInSAR technique [25,26], which allows the analysis of the surface displacement, by providing a measurement of the ground deformation projection along the radar line-of-sight (LoS). The SAR data considered to retrieve the ground deformation associated with the occurred seismic event were acquired by the Sentinel-1 (S1) constellation of the Copernicus European Programme, along both the descending (Track 78) and ascending (Track 71). In Figure 3, we show the location of the earthquake epicentre (identified by a red star), the cover area for both orbits and the co-seismic LoS displacement maps. In Table 1, instead, we reported several types of data about the exploited interferometric pairs. In particular, the generated differential interferograms underwent a multilook operation (5 and 20 pixels along the azimuth and range directions, respectively) to finally lead to a ground pixel size of about 73 by 73 m. Subsequently, we generated their corresponding LoS displacement maps through the minimum cost flow phase unwrapping procedure [27,28]. Moreover, for sake of completeness, it is important to highlight that the differential interferograms and the corresponding LoS displacement maps were automatically generated by an unsupervised tool from DInSAR products [29] and made available on the European Plate Observing System (EPOSAR) service through Thematic Core Service (TCS) of Satellite Data (EPOS 2023).

As described in Table 1, we benefited from the short revisit time (12 days) and the small spatial/perpendicular baseline separation of the S1 constellation to generate two interferograms for each orbit by using different primary acquisitions (see Figure 3). Among them, for the seismic source modelling discussed in the following sections, we selected those least affected by undesired phase artefacts (e.g., atmospheric phase delays, decorrelation noise), thereby optimizing the reconstruction of the deformation pattern affecting the area (Figure 3a). In particular, the employed S1A data were acquired on 19 June and 1 July 2022 and on 18 June and 30 June 2022 along the descending and ascending orbits, respectively. Moreover, by exploiting these displacement maps generated from ascending and descending displacement analysis, it was possible to compute the vertical and east–west displacement components [30–32]. The corresponding results are shown in Figure 4. In further detail, the displacement component maps reveal a maximum deformation of 27 cm of uplift and 10 cm of subsidence (see Figure 4b), while the east–west displacement indicates a maximum of 35 cm toward to the east and 14 cm toward to the west (see Figure 4a).

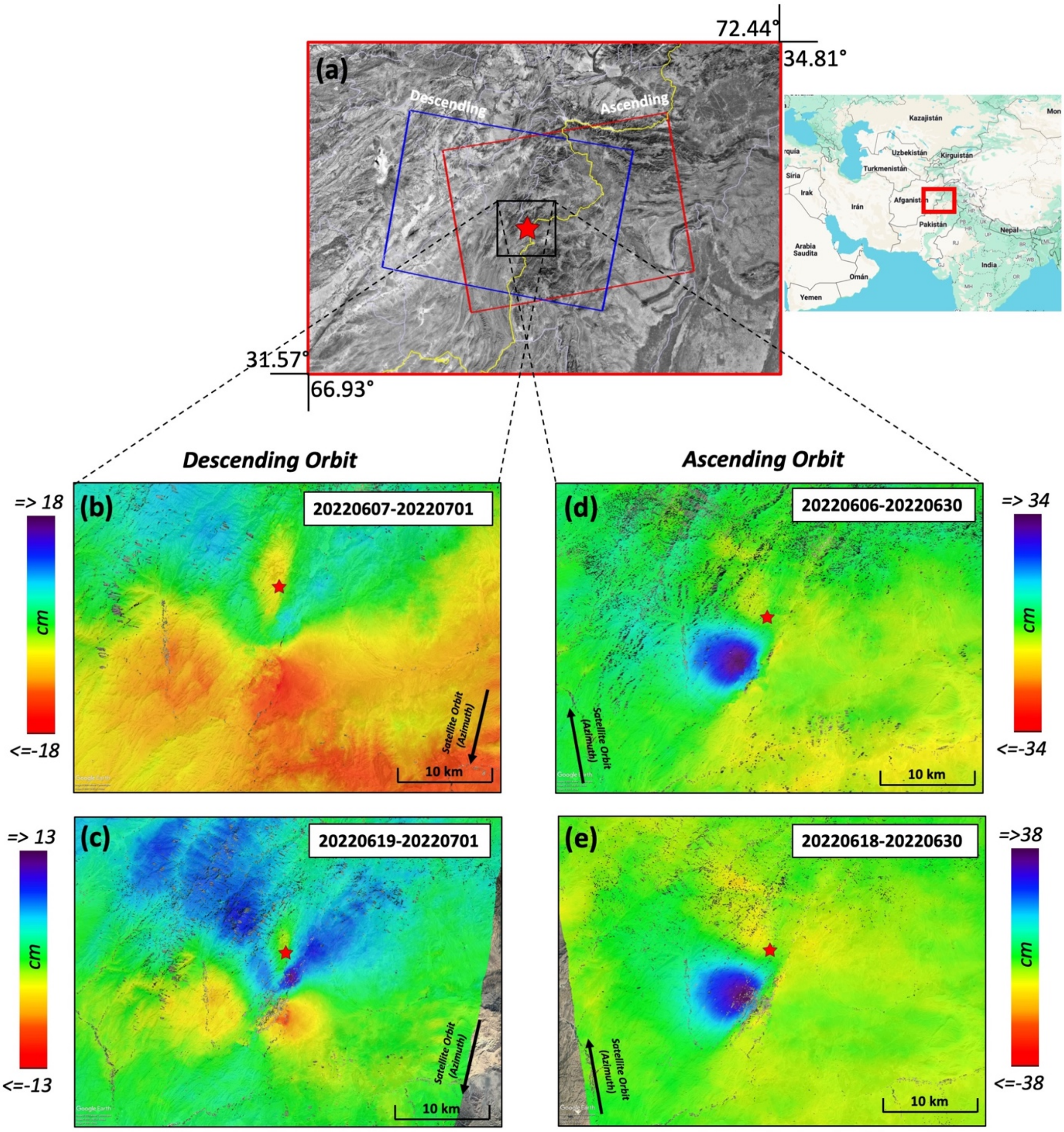

Figure 3. Sentinel-1A coseismic LoS displacement results relevant to the 21 June 2022 earthquake in Eastern Afghanistan: (**a**) indicates the Sentinel-1A footprints used to cover the area of interest (ascending orbit red line and descending orbit blue line); (**b**,**c**) show the coseismic LoS displacement maps for the descending orbit; (**d**,**e**) show co-seismic LoS displacement maps for the ascending orbit. Earthquake epicentre is shown by the red star.

Table 1. Main characteristics of the interferometric pairs considered for the seismic source modelling of the Mw 6.0 earthquake in the southwest of Khost, Afghanistan.

Sensor	Primary-Secondary	Orbit	Track	Perpendicular Baseline [m]
Sentinel-1A	6 June 2022–30 June 2022 18 June 2022–30 June 2022	Ascending	71	−15.1934 −165.464
	19 June 2022–1 July 2022 7 June 2022–1 July 2022	Descending	78	−76.3265 −7.78262

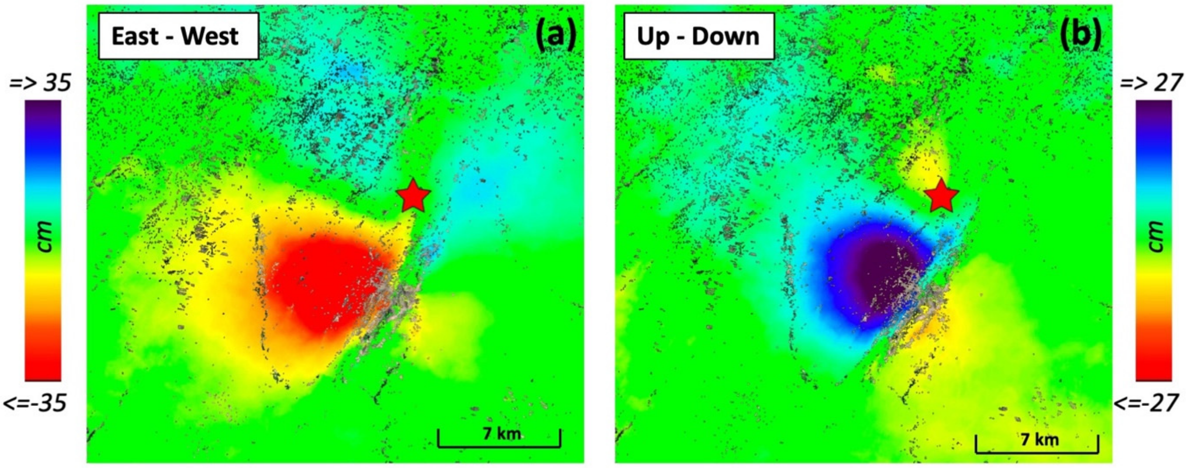

Figure 4. Horizontal (east–west) and vertical (up–down) displacement component of coseismic results relevant for the 21 June 2022 earthquake in eastern Afghanistan: (**a**) east–west and (**b**) up–down coseismic displacement maps, respectively. Earthquake epicentre is shown by the red star.

The InSAR measurements and fault modelling results (presented in Table 2) compare well with the already available results [6,33–35]. However, there are fine differences, which may be mainly due to the differences in downsampling strategies and the boundary conditions input to arrive to the model results.

Table 2. Existing fault model results from previous studies compared to this study.

Parameters	USGS	GCMT	GFZ	IPGP	[33]	[34]	[35]	[6]	This Study
Epicentre	33.02° N 69.46° E	32.94° N 69.51° E	33.10° N 69.5° E	33.11° N 69.53° E	-	69.46° N 32.99° E	-	33.0° N 69.5° E	33.01° N 69.46° E
Magnitude (Mw)	6.02	6.2	6.1	6.2	5.99	6.32	6.18	6.18	6.2
Strike	204°	202°	104°	220°	218°	203.7°	216°	212.75°	214.41°
Dip	87°	57°	89°	70°	72.8°	68°	61.9°	72.04°	80°
Rake	−11°	10°	165°	−3°	-	6.9°	-	14.08°	24.9°
Depth (Km)	11.5	15.5	10	6	7.1	2.5	-	4.92	3.56
Slip (m)	0–1.5	-	-	-	1.05	0–3	0–2.26	1.91	0–3
Length (Km)	-	-	-	-	7.5	20	-	5.91	10.33
Width (Km)	-	-	-	-	6.0	12	-	-	9

4. Results

4.1. Geology/Geomorphology

The geological maps show that the 21 June 2022 earthquake occurred along the easternmost section of the Katawaz Basin (KB) where it forms the North Waziristan—Bannu fault system and juxtaposes with the northern closure of the Sulaiman Range (SR). The tectonic contact, KB/SR, along this section becomes almost sub-parallel to the CF, which is part of the larger CTZ (Figure 2). It is optimally oriented to accommodate part of the left-lateral plate motion between India and Eurasia. It is worth to note that this section is also included in the active fault database [19], where a fault segment with a slightly curved geometry, concave towards the west, likely corresponds to the causative fault of the earthquake (Figures 5 and 6).

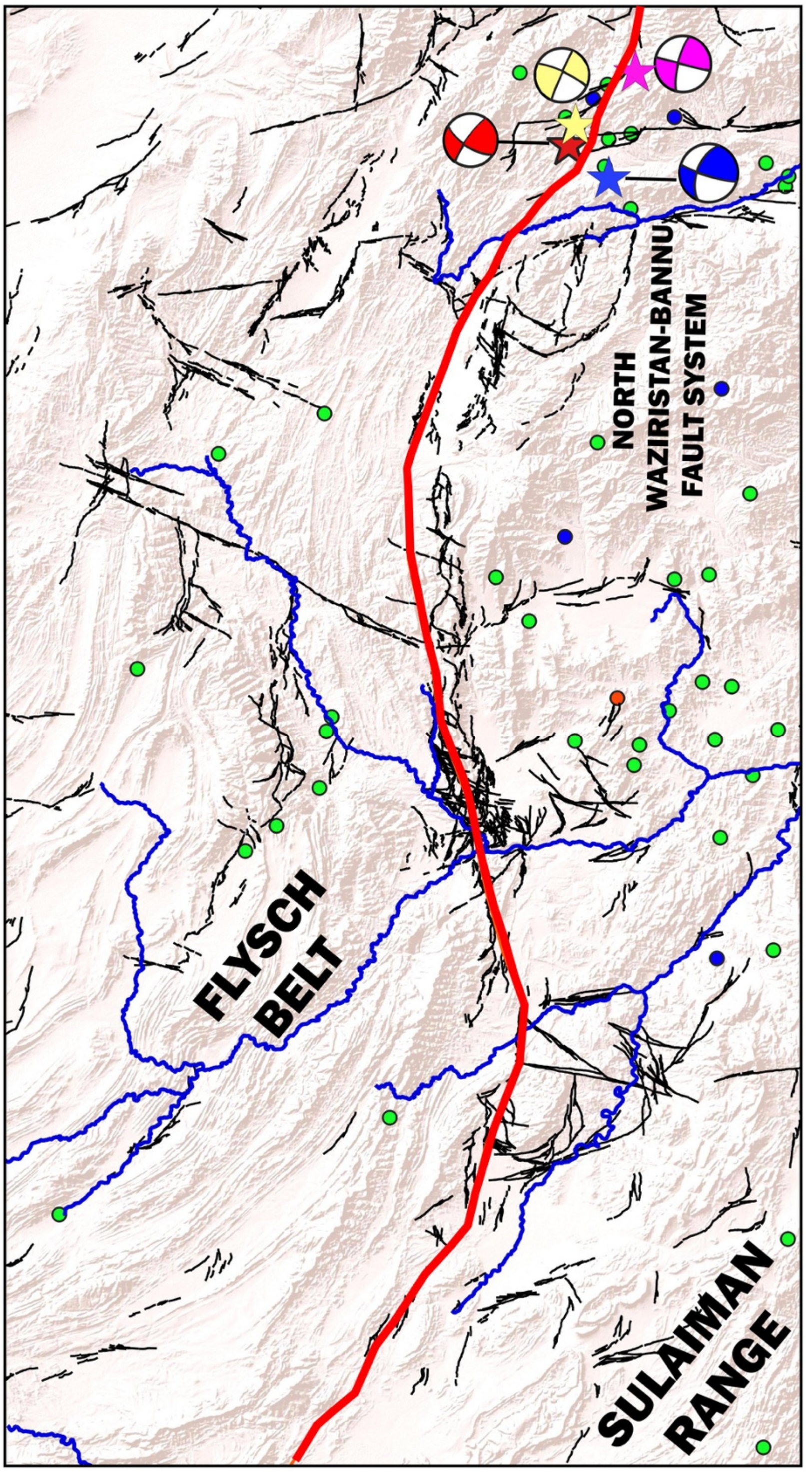

Figure 5. Red line shows that general trace of the fault separating the flysch belt of the Katawaz Basin in the west, which forms the NWBFS towards the north, from the Sulaiman Range in the east. The 21 June 2022 event is shown by the star symbol. Stars represent epicentres with focal mechanisms from different agencies: yellow (USGS), pink (GFZ), blue (GCMT) and red (this study). Black lines are active fault segments from Ruleman et al. [6]. Dots represent minor seismicity. For the location, refer to Figure 2.

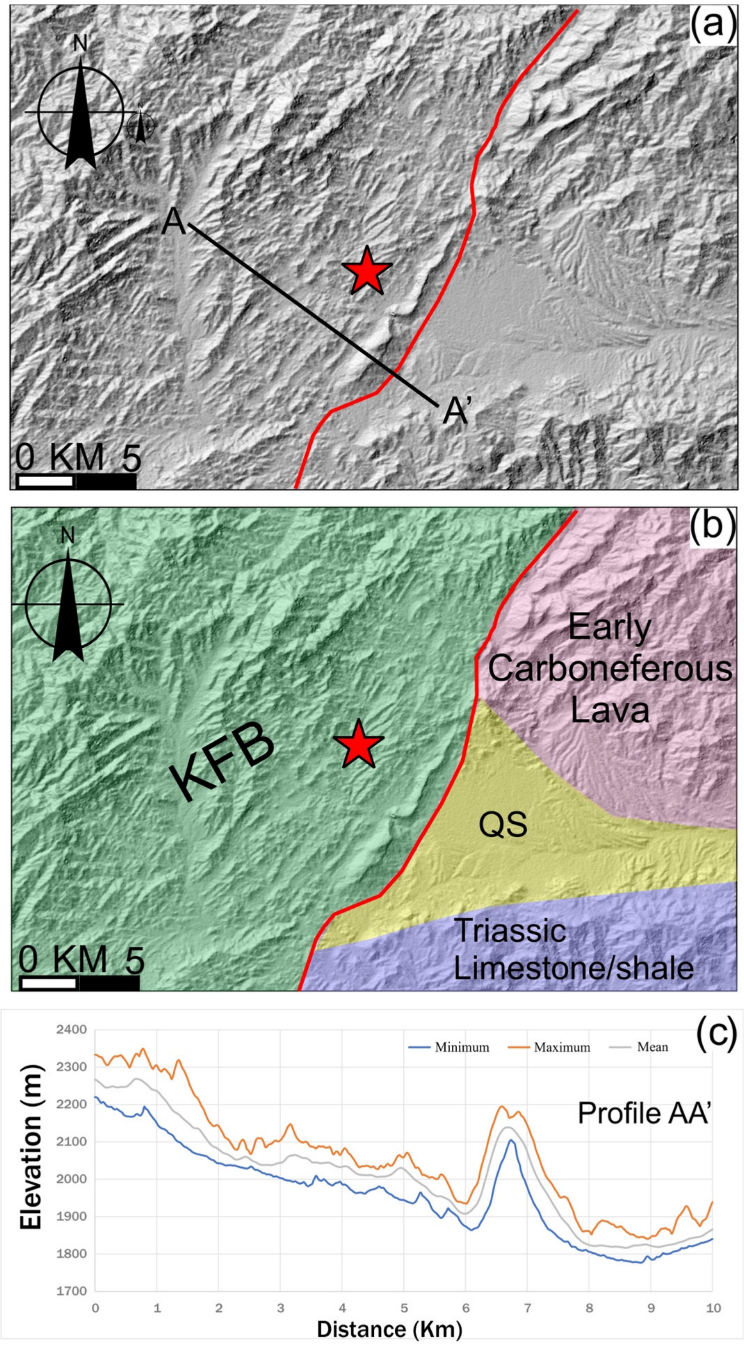

Figure 6. Generalized setting of the epicentral region of the 21 June 2022 earthquake (marked by the red star). The red line conforms to the trace of the active fault (**a**) DEM highlighting the abrupt rise in the ridge along the bend of the fault. (**b**) Geological map showing the ridge directly abutting against the Quaternary sediment (QS). (**c**) Swath profiles display the abrupt rise in the ridge in comparison to the surrounding topography. Profile line is A-A′.

The fault trace makes a discontinuous lineament that extends over 100 km riddled with numerous active fault segments (Figure 5). Particularly, the fault segment responsible for the 21 June 2022 event displays an abrupt bend in the lineament, and also a pronounced ridge topography trending nearly parallel to the active tectonic structure (Figures 5 and 6). The NNE-SSW trending ridge forms a discernible topographic front that abruptly rises ~300 m above the gently sloping plain of unconsolidated Quaternary sediments on the east (Figure 6). The topographic front is characterized by discontinuous, linear, north–northeast-trending scarps located towards the top. On the images, the discontinuous scarps present a bright signature, suggesting them to be relatively fresh, likely due to the ongoing tectonic activity and the consequent rejuvenation of the morphological feature (Figure 7a). As seen on the DEM, the width of the ridge appears to gradually increase to ~2 km through the central part towards the south, where it displays the maximum elevations of ~2200 m (Figure 6). The ridge effectively obstructs the drainage which takes courses parallel to the trend of the ridge, except for the exit where the adjoining parallel streams join cutting across the relief.

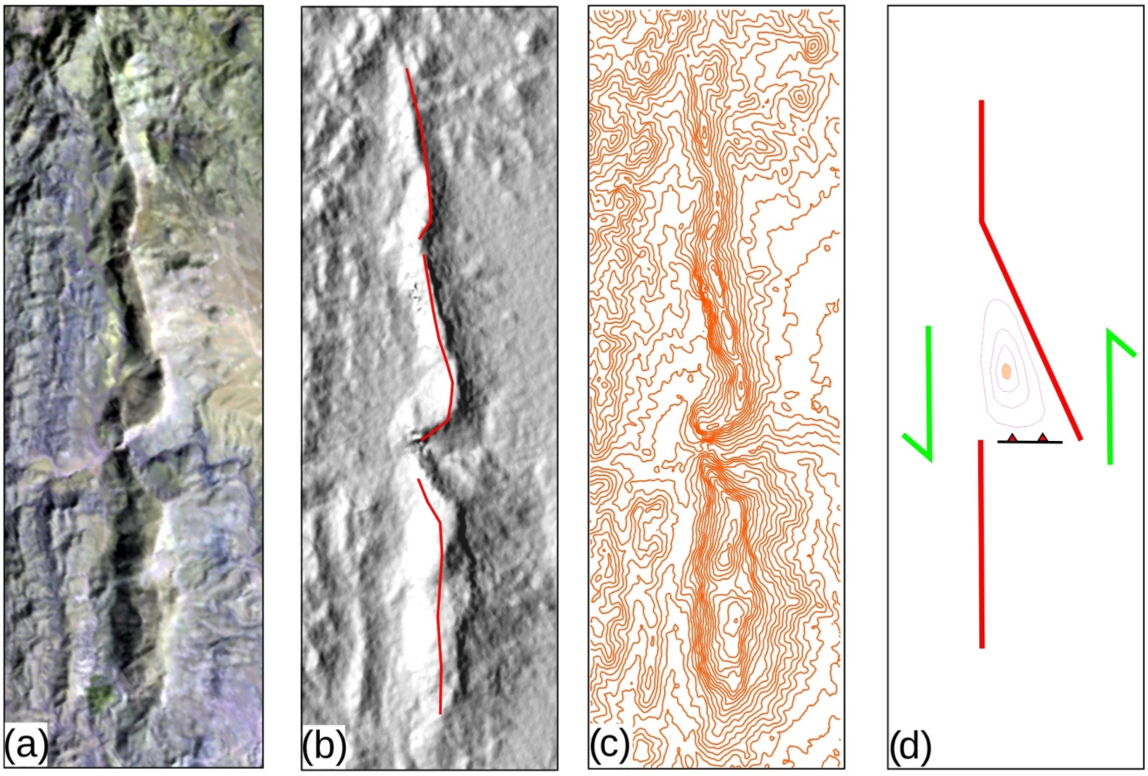

Figure 7. The arrangement of right-stepping fault bends forming a segmented ridge topography in a left-lateral environment: (**a**) as seen on satellite image; (**b**) as seen in DEM, the red lines follow the ridge top; (**c**) contours (5 m) for better visualization of topography; and (**d**) schematic model showing evolution of the observed fault bend and related ridge topography across the fault step-overs. The contours inside the bend show the ridge topography (high in the centre).

The multi-resolution satellite imageries were studied to explore the epicentral region. It is observed that the topographic ridge corresponding to the active fault is locally deviated slightly from the general trend of the corresponding longer lineament forming a conspicuous bend in the fault, which is concave towards the west (Figures 5 and 6). High-resolution IRS images show that the ridge is basically made of smaller discontinuous bends arranged in a typical en-echelon geometry, where the segments are arranged in a right-stepping fashion (Figure 7). The right-stepping en-echelon segments in a left-lateral environment tend to form compressional step-overs and restraining bends that produce the discontinuous but positive topography of the ridge (Figure 7).

4.2. InSAR Analysis

The area of eastern Afghanistan and Western Pakistan is generally devoid of any significant vegetation, so it is expected to return good coherence across various times. However, the earthquake caused significant ground motion and damage to property and infrastructure [5,33], causing an exceptional loss of coherence along the fault line in the epicentral region (Figure 8). Accordingly, it should be expected that the details of fault slip/geometry closer to the fault on a length scale of 1–2 km may be poorly resolved due to an important loss of coherence. This limitation may have some interesting implications on resolving the fault structure, and this is discussed in a following section.

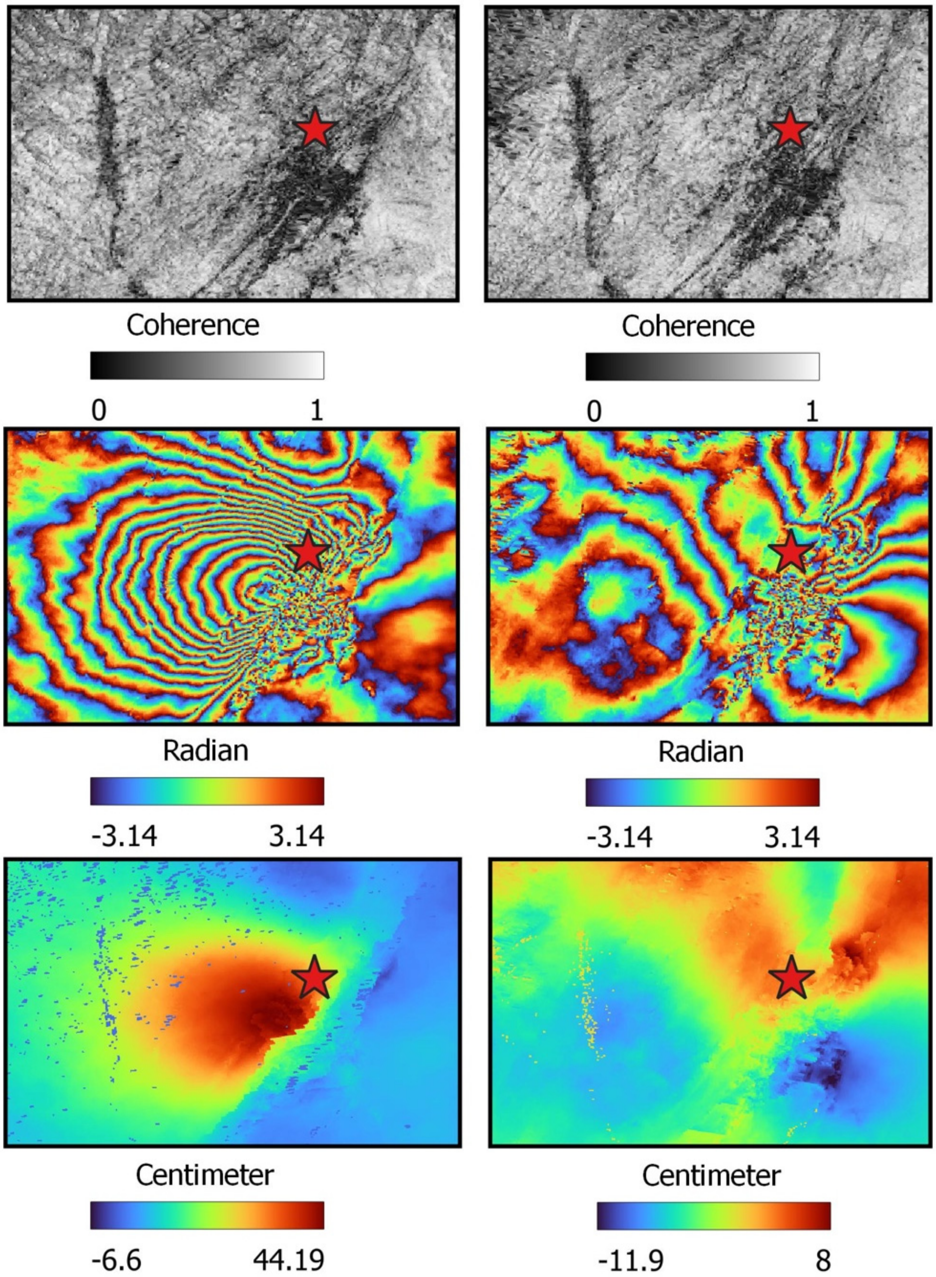

Figure 8. InSAR results for the 21 June 2022 earthquake, USGS epicentre shown by the red star. Results from the ascending mode (**left** panel) and descending mode (**right** panel). Coherence maps (**top** panel), phase change fringes (**middle** panel), and LoS displacement (**bottom** panel).

The interferometric processing of the master (pre-event) and slave (post-event) SAR imageries (Table 1) produced co-seismic interferograms for ascending and descending modes (Figure 8). The interferograms were unwrapped and phase change was converted into range change to ascertain the line-of-sight (LoS) displacement in both cases (Figure 8). The fault trace can be seen in both interferograms by the geometry of the fringes and lobes of LoS displacement with abrupt truncation along the fault line. The change in signature of displacement values from positive (away from the satellite) to negative (towards the satellite) allows the fault and its geometry to be constrained. The ascending mode interferograms capture a very clear fault trace nearly parallel to the active fault proposed by Ruleman et al. [3], but slightly shifted to the west by ~1–2 km. The descending mode interferogram captures a more complex trace, perhaps due to the SAR imaging geometry and complex fault geometry [6,35]. However, the deformation pattern mainly suggests a strike slip faulting with left-lateral kinematics.

To further constrain the fault geometry and slip parameters, we performed a joint inversion of the ascending and descending mode interferograms. For the model, the original data are downsampled where a denser sampling interval is taken near the source of deformation and a coarser sampling interval is taken away from the source region. The downsampled input data were inverted using a distribution slip model with 360 patches [36]. The derived fault model shows that the earthquake was a shallow event (~4 km-deep), and the fault rupture stopped at a shallow depth of less than 1 km, suggesting no primary surface rupture (Figure 9). The fault strikes 212–218° and dips sub-vertically, i.e., 78–80° due west. The maximum slip is constrained at 3 m, with a mean slip of 1 m. We found a significant improvement in data–model correlation during the joint inversion of the ascending and descending datasets, which compensated for the fault orientation and the SAR viewing geometry (Table 3). The estimated magnitude is 6.2.

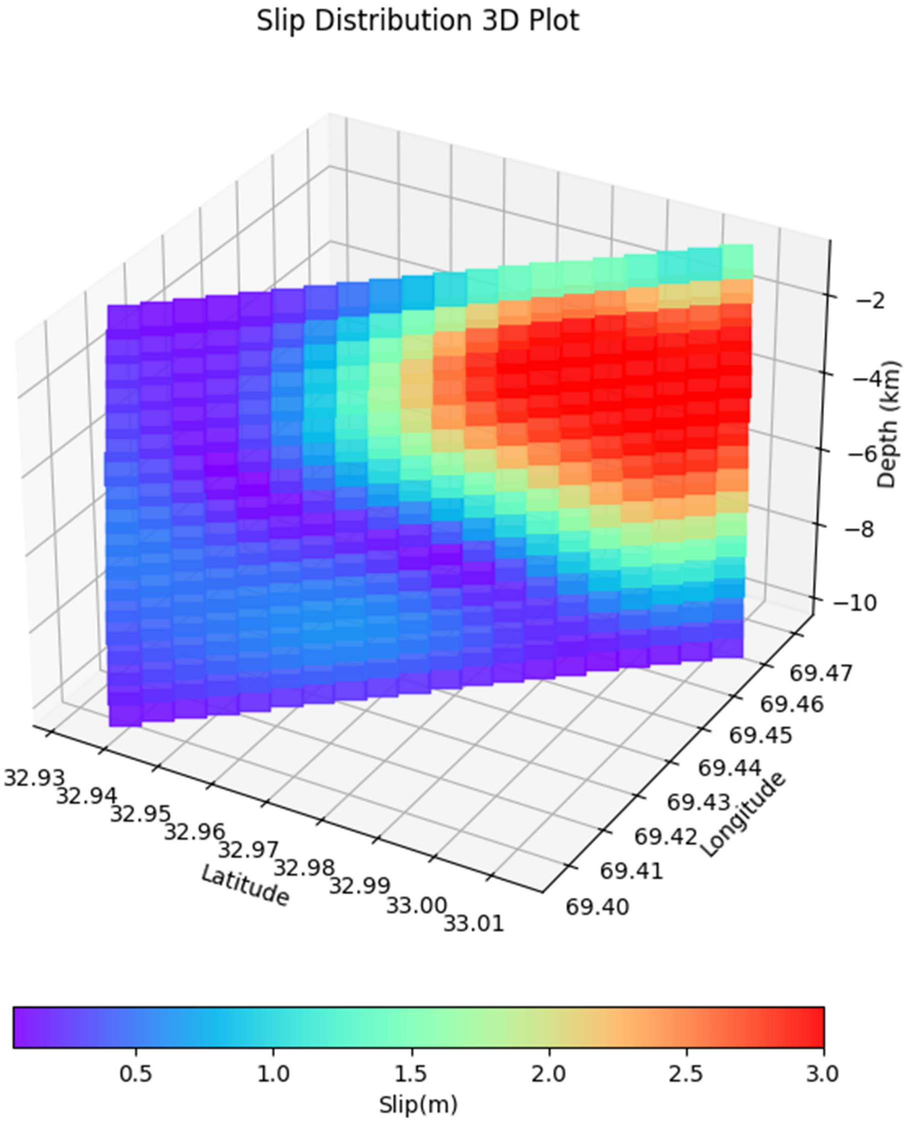

Figure 9. 21 June 2022 Afghanistan earthquake fault model showing variable slip distribution along the fault plane.

Table 3. The model parameters for ascending, descending and joint inversion (data to be added).

Latitude (degree)	33.01
Longitude (degree)	69.46
Magnitude	6.2
Depth (Km)	3.56
Length (Km)	10.33
Width (Km)	9
Strike (degree)	214.41
Dip (degree)	80
Mean slip (metre)	1.08
Max slip (metre)	3
Rake (degree)	25
Data–model correlation	0.87

5. Discussion

Based on the study of geological and geomorphic evidence, it appears that the surface manifestation of the active fault responsible for the 21 June 2022 Afghanistan earthquake closely follows the geological boundary between the Katawaz flysch basin (KFB) and the Sulaiman Range (SR) towards its northern closure into the North-Waziristan-Bannu fault system (Figure 5). In this segment, the fault becomes sub-parallel to the Chaman fault and is favourably oriented to accommodate a part of the differential motion between the Indian and Eurasian plate. Interestingly, the boundary corresponds to an already identified active fault segment based on landform mapping and geomorphic feature offsets [19]. These observations are also supported by the active fault topographic features elaborated in the Results section (Figures 5 and 6). Based on the data presented here, it is notable that the active fault presents a typical curvature/bend concave towards the west which encloses a sharp topographic ridge on its western side. Due to the earthquake, landslides were clustered all around the ridge [6]. It is noticeable that the fault curvature/bend is an offset from the main fault and corresponds well to the width of the ridge. The ridge becomes wider in the south–central part and swiftly narrows down towards its northern termination, forming an en-echelon pattern of ridges (Figure 7). Such en-echelon patterns are typical of fault step-overs [37]. In this case, the step-overs formed restraining bends thus generating push-up ridges. It is well known that the strong compression near the inside corners of these restraining bends cause increased uplift rates forming sharp ridges [38,39]. The spatial correspondence of all the above manifestations suggests a strong connection between the seismogenic fault and surface topography (Figures 6 and 7).

At the same time, the co-seismic interferograms show a perfect linear fault trace, with clear lobes of different LoS displacements (Figure 8). Although the InSAR fault trace is slightly offset (~1–2 km westwards) relative to the morphotectonic evidence, the two have almost the same average strike and correspond well with the length of the sharp topographic ridge (Figures 5 and 6). Following the slip model, the fault terminates upwards at a shallow depth of about 1 km, and it does not reach the surface (Figure 9). Considering this information, it is seen that the InSAR LoS displacements and topographic profiles show the corresponding maxima towards the south–central part of the ridge, where the ridge attains its maximum width and elevation (Figures 5 and 6). The LoS displacements tend to reduce northwards along the fault line and appear to follow the narrowing topography of the ridge (Figures 7 and 10). A similar observation has been reported based on the coherence maps which suggest a wider damage zone in the south–central part [33].

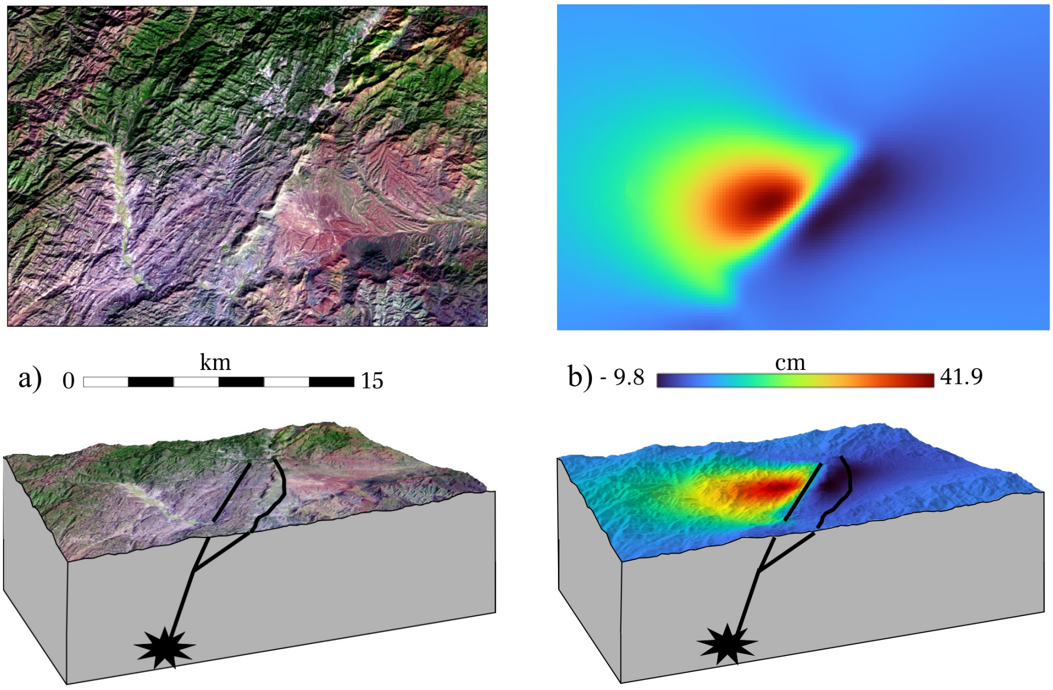

Figure 10. The (**top**) panel shows the active fault derived from (**a**) surface topography and (**b**) co-seismic LoS displacements. The (**lower**) panel shows the respective 3D perspective views of the active fault derived from (**a**) surface topography and (**b**) co-seismic LoS displacements. The star shows the focus of the earthquake and the black bold lines in section view are sub-surface reconstructions of the active faults.

The previous arguments suggest that the active fault derived from the morphotectonic analysis is slightly offset from the one derived on the basis of the co-seismic LoS displacements (Figure 10). This may be primarily due to two reasons: (i) InSAR was unable to capture the deformation geometry in the area closer to the surface fault. This could be due to loss of coherence caused by the severe shaking and the randomly distributed surface deformation, as also seen by severe landsliding along the ridge crest. (ii) The fault geometry changed near to the surface as the fault model is unable to capture any surface rupture. In the shallow sub-surface, the faults commonly tend to either follow local geological discontinuities or any other inherited weakness zone.

Further, as inferred from the very few ground reports [33], a series of secondary features such as landslides, building damage, fractures, syn- and antithetic Riedel shears have been identified in the field. However, no reports of any primary surface rupture are available, similarly to the fault modelling results (Table 3). As most of these sites are at least 1.5 km west of the InSAR fault trace, they do not offer any direct insights into the fault setting and geometry. Moreover, InSAR results and model calculations suffer from the coherence loss in the area related to the fault line. Therefore, it could be reasonably assumed that the InSAR technique is able to capture the general geometry of the fault at depth where it is continuous and relatively smooth. However, it is unable to capture it at close range and shallow depth. This is where a morphotectonic approach becomes important and any deviation between the two fault traces may arise due to geological complexities and/or InSAR method limitations. Indeed, based on our own analyses and fault model, it is likely that no primary surface rupture has occurred during this earthquake. This major conclusion and a similar fault geometry and kinematics, i.e., subvertical fault surface with sinistral slip ([6,33–35] and this study), could be reasonably reached based on the secondary field evidence and modelling results. It is also important that as the fault does not rupture to the surface, the deformation patterns have to be judiciously interpreted using secondary effects, which are commonly controlled by the local geological conditions.

Interestingly, the field observations are limited to the western part of the InSAR fault trace and there is no real ground information from the eastern sector near to the active fault trace of [6]. This leaves an interpretative uncertainty that could be a priority in future research. However, considering this limitation, a combination of the geologic/geomorphic observations with the InSAR measurements provide useful insights, as discussed hereon (Figures 8 and 10). It is revealed that the geologic/geomorphic active fault is located ~1–2 km east of the InSAR fault trace (Figure 10), where there is a cluster of landslides on the ridge [6,35] corresponding to the area of coherence loss ([6] and this study). Although the InSAR fault trace corresponds to the maximum change in LoS displacements on either side surrounded by a pronounced zone of coherence loss, there is absence of any corresponding discernible topographic manifestation (Figures 6, 7 and 10). Conversely, the active fault trace of [3] bears the most discernible active fault features: (i) fresh cluster of landslides on the ridge and (ii) bends in the ridge typical of left-lateral kinematics. Most importantly, these two ridge anomalies correspond to the continuous zone of coherence loss along the ridge (Figure 8).

Accordingly, it is inferred that the InSAR fault trace is slightly offset from the morphotectonic feature; it may represent two aspects of the same fault. The InSAR-based fault model represents the broader sub-surface geometry of the fault plane matching the co-seismic LoS deformation pattern (Figures 10 and 11). This fault-plane is blind and does not actually rupture the surface. On the contrary, the observed morphotectonic feature represents the shallow evidence of the same structure that could slightly deviate from the broader sub-surface geometry due to the fact that the confining pressure decreases upwards and repeated ruptures could occur along more variable paths. This could allow the fault to deviate from an ideally flat geometry and, instead, follow local geological heterogeneities, like layering or structural discontinuities. In case of transcurrent faulting, similar local variations commonly give rise to releasing or restraining bends [39–43]. In this regard, the deviation between the InSAR and geologic/geomorphic fault traces for the investigated case corresponds with such a bend along the strike, where the geometry of the fault suggests the occurrence of a right stepping left-lateral structure which is expected to produce local uplift with the formation of a pop-up ridge within the restraining bend (Figures 6 and 7). Towards the north, the restraining bend disappears along the fault trace, thereby confining the ridge, which is wider in the southern and central part and narrows down northwards (Figures 6 and 7). Such subtle but possible correlation between the topographic features and the bend along the fault strike might have been missed by the InSAR technique mainly due to the local coherence loss, the geometry of imaging, and/or the blind nature of the fault.

In summary, it is proposed that in the shallow sub-surface, i.e., up to ~1–2 km, the fault plane is sub-vertical due to large confining pressures from the adjoining fault blocks. However, the situation changes significantly in the near-surface, where the reduced overburden and confining pressure is considerably reduced. The fault is unable to maintain itself in the same plane; rather, it takes preferential paths along pre-existing geological discontinuities, such as the rock foliation, that coincide with the fault strike, as reported from sites recorded by [3,6], but with gentler dips (~30–60°) westward. Such a change/bend in the fault strike forms a geometrical complexity, making a restraining bend which is manifested by the topographic ridge. The restraining bend acts as a subtle barrier that can effectively hinder slip on the fault plane causing high-strain zones [41,44]. The model results also show increased deviatoric stress and high strain rates around fault stepovers and restraining bends [37]. Fault stepovers localize strain and they have been identified as loci of both initiation and termination for seismic ruptures [43,44]. This suggests that such step-overs play an important role in controlling the size and extent of earthquakes, and consequently the seismic hazard around strike-slip fault zones [44,45].

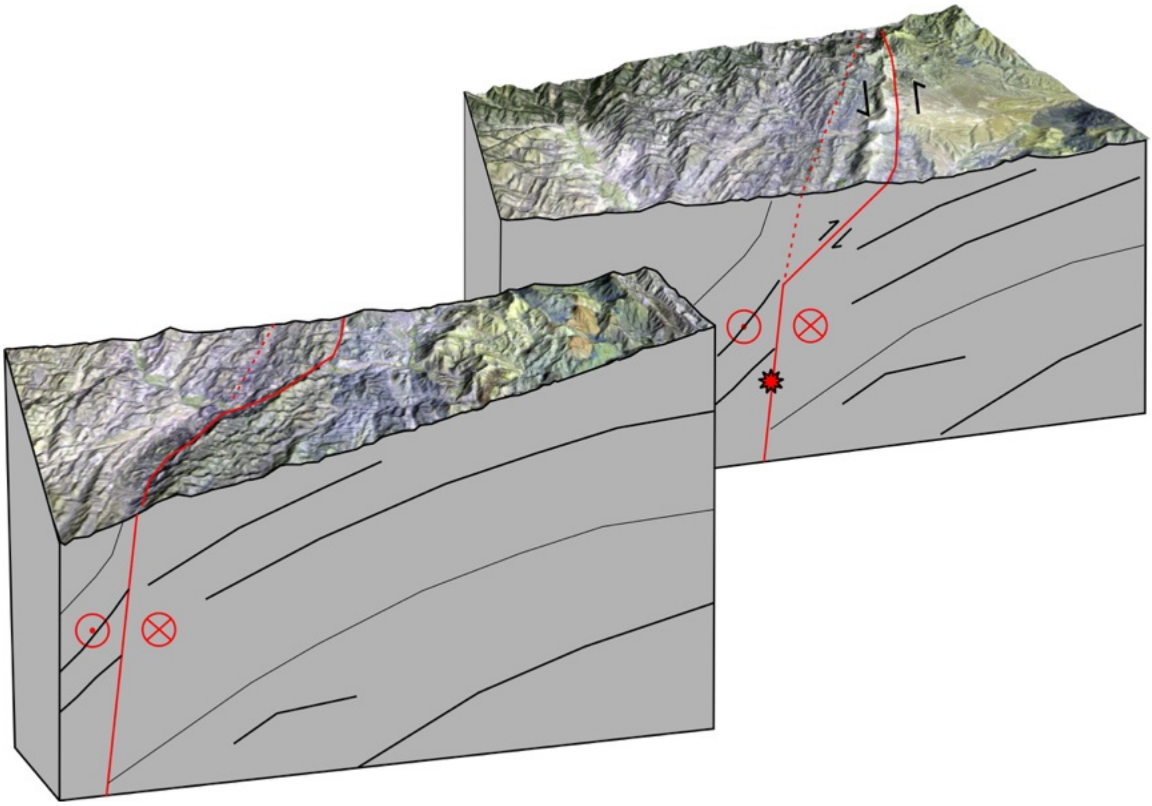

Figure 11. A schematic 3D perspective of the fault geometry. The two blocks contain the same fault line but have been offset only to help better visualization of the fault geometry in the sub-surface and near-surface. The offset of blocks does not represent the movement along the fault. The actual fault geometry inferred from this study is shown as a continuous red line in the section view, that deviates from the InSAR faultline (shown as dashed red line). Other symbols are standard fault movement representing a left-lateral kinematics.

6. Conclusions

The modelled geometry of the active fault from the InSAR measurements is consistent with the style of deformation inferred from the satellite remote sensing and DEM datasets used in this study, and that determined from focal mechanisms by various other agencies (USGS, etc.)

It is surmised that the primary earthquake genesis and faulting at depth are guided by the structural geometry where the typical compressional fault stepovers contribute significantly to concentrating the tectonic strain, and the rapid uplift of surface topography along the ridge.

Author Contributions: Conceptualization, T.S., R.C., C.D.L. and C.P.R.; methodology, T.S. and R.C.; software, T.S., N.N., F.M. and P.S.; validation, T.S., N.N., F.M. and P.S.; formal analysis, T.S., N.N., F.M., P.S. and C.D.L.; investigation, T.S., N.N., F.M., P.S. and C.D.L.; resources, T.S., R.C., C.D.L., R.L. and C.P.R.; data curation, T.S., N.N., F.M. and P.S.; writing—original draft preparation, T.S., N.N. and R.C.; writing—review and editing, T.S., R.C., C.P.R., C.D.L., R.B.S.Y. and A.G.S.; visualization, T.S., N.N., C.D.L. and R.C.; supervision, T.S., R.C., C.P.R., R.L. and R.B.S.Y.; project administration, T.S., R.C. and A.G.S.; funding acquisition, T.S. and R.C. All authors have read and agreed to the published version of the manuscript.

Funding: This research was funded by the India–Italy Bilateral Programme supported by the Department of Science and Technology (DST), Government of India and the Italian Ministry for Foreign Affairs and International Cooperation (MAECI).

Data Availability Statement: All data used in this study are publicly available. The source is mentioned within the article and properly cited.

Acknowledgments: The work is an outcome of the India–Italy Bilateral Programme supported by the Department of Science and Technology (DST), Government of India and the Italian Ministry for Foreign Affairs and International Cooperation (MAECI). This research was also partially funded by the European Union—NextGeneratonEU through the following projects: ICSC–CN-HPC–PNRR M4C2 Investimento 1.4—CN00000013, GeoSciences IR–PNRR M4C2 Investimento 3.1— IR0000037 and CN-MOST–PNRR M4C2 Investimento 1.4—CN00000023. CSIR-Central Scientific Instruments Organization Chandigarh and National institute of Advanced Studies Bengaluru acknowledge funding was from the DST vide grant no. INT/Italy/P-46/2022(SR), while the University of Ferrara and Italian National Research Council acknowledge funding by MAECI. NN was supported by a fellowship from the Ministry of Earth Sciences, Government of India vide grant no. MoES/PO/(Seismo)/1(342)/2019.

Conflicts of Interest: The authors declare no known conflicts of interest.

List of Acronyms

InSAR	Interferometric Synthetic Aperture Radar
LoS	Line-of-sight
AMF	Alburz Marmul fault
AF	Andrab fault
BTF	Bande Turkestan fault
CBF	Central Badakhshan fault
CF	Chaman fault
DMF	Dosi Mirzavalang fault
GF	Gardiz fault
HF	Herat fault
KF	Konar fault
MF	Mokur fault
SGF	Spin Ghar fault
SR	Salt Range
KB	Kashmir basin
PB	Peshawar basin
PP	Potwar plateau
SF	Sagaing fault
USGS	United States Geological Survey
GCMT	Global Centroid Moment Tensor
GFZ	GeoForschungsZentrum (Geo-Research Centre)
IPGP	Institut de Physique du Globe de Paris

References

1. Reynolds, K.; Copley, A.; Hussain, E. Evolution and dynamics of a fold-thrust belt: The Sulaiman Range of Pakistan. *Geophys. J. Int.* **2015**, *201*, 683–710. [CrossRef]
2. Jouanne, F.; Pousse-Beltraltn, L.; Doin, M.P.; Bascou, P.; Thollard, F.; Ahmed, A. Current tectonic deformation of the Sulaiman range (Pakistan) with InSAR. *Geophys. J. Int.* **2025**, *240*, 2060–2075. [CrossRef]
3. Ruleman, C.A.; Crone, A.J.; Machette, M.N.; Haller, K.M.; Rukstales, K.S. Map and Database of Probable and Possible Quaternary Faults of Afghanistan. U.S. Geological Survey Open-File Report 2007-1103. 2007. Available online: https://pubs.usgs.gov/of/2007/1103/downloads/pdf/of07-1103_508.pdf (accessed on 22 February 2024).
4. Treloar, P.J.; Izatt, C.N. Tectonics of the Himalayan collision between the Indian plate and the Afghan block: A synthesis. *Geol. Soc. Lond. Spec. Publ.* **1993**, *74*, 69–87. [CrossRef]
5. Mallapaty, S. Deadly Afghanistan quake challenges scientists trying to study it. *Nature* **2022**, *607*, 433. [CrossRef]

6. Kufner, S.; Bie, L.; Gao, Y.; Lindner, M.; Waizy, H.; Kakar, N.; Rietbrock, A. The Devastating 2022 M6.2 Afghanistan Earthquake: Challenges, Processes, and Implications. *Geophys. Res. Lett.* **2023**, *50*, e2022GL102176. [CrossRef]
7. Roy, P.; Martha, T.R.; Kumar, K.V.; Chauhan, P. Coseismic deformation and source characterisation of the 21 June 2022 Afghanistan earthquake using dual-pass DInSAR. *Nat. Hazards* **2023**, *118*, 843–857. [CrossRef]
8. Lawrence, R.D.; Khan, S.H.; Nakata, T. Chaman Fault, Pakistan-Afghanistan. *Ann. Tectonicae Spec. Issue Suppl.* **1992**, *VI*, 196–223.
9. McCaffrey, R. Oblique plate convergence, slip vectors, and forearc deformation. *J. Geophys. Res.* **1992**, *97*, 8905–8915. [CrossRef]
10. Yu, G.; Wesnousky, S.G.; Ekström, G. Slip partitioning along major convergent plate boundaries. *Pure Appl. Geophys.* **1993**, *140*, 183–210. [CrossRef]
11. Bowman, D.; King, G.; Tapponnier, P. Slip Partitioning by Elastoplastic Propagation of Oblique Slip at Depth. *Science* **2003**, *300*, 1121–1123. [CrossRef]
12. Crupa, W.E.; Khan, S.D.; Huang, J.; Khan, A.S.; Kasi, A. Active tectonic deformation of the western Indian plate boundary: A case study from the Chaman Fault System. *J. Asian Earth Sci.* **2017**, *147*, 452–468. [CrossRef]
13. Szeliga, W.; Bilham, R.; Kakar, D.M.; Lodi, S.H. Interseismic strain accumulation along the western boundary of the Indian subcontinent. *J. Geophys. Res.* **2012**, *117*, B08404. [CrossRef]
14. Dalaison, M.; Jolivet, R.; van Rijsingen, E.M.; Michel, S. The Interplay Between Seismic and Aseismic Slip Along the Chaman Fault Illuminated by InSAR. *J. Geophys. Res. Solid Earth* **2021**, *126*, e2021JB021935. [CrossRef]
15. DeMets, C. Plate motions and crustal deformation. *Rev. Geophys.* **1995**, *33*, 365–369. [CrossRef]
16. Bilham, R.; Gaur, V.K.; Molnar, P. Himalayan Seismic Hazard. *Science* **2001**, *293*, 1442–1444. [CrossRef]
17. Banerjee, P.; Bürgmann, R.; Nagarajan, B.; Apel, E. Intraplate deformation of the Indian subcontinent. *Geophys. Res. Lett.* **2008**, *35*, L18301. [CrossRef]
18. Dalaison, M.; Jolivet, R.; Le Pourhiet, L. A snapshot of the long-term evolution of a distributed tectonic plate boundary. *Sci. Adv.* **2023**, *9*, eadd7235. [CrossRef]
19. Tapponnier, P.; Mattauer, M.; Proust, F.; Cassaigneau, C. Mesozoic ophiolites, sutures, and arge-scale tectonic movements in Afghanistan. *Earth Planet. Sci. Lett.* **1981**, *52*, 355–371. [CrossRef]
20. Shnizai, Z. Active Tectonics and Seismic Hazard Assessment of Afghanistan and Slip-Rate Estimation of the Chaman Fault Based on Cosmogonic 10Be Dating. Ph.D. Thesis, Doshisha University, Kyoto, Japan, 2020; p. 126.
21. Shnizai, Z.; Walker, R. Detailed Active Fault Map of the Spin Ghar Fault System and Related Seismicity in Eastern Afghanistan. *Tektonika* **2024**, *2*, 132–156. [CrossRef]
22. Burbank, D.W.; Anderson, R.S. *Tectonic Geomorphology*; Blackwell: Kay County, OK, USA, 2011.
23. Duvall, A.R.; Tucker, G.E. Dynamic Ridges and Valleys in a Strike-Slip Environment. *J. Geophys. Res. Earth Surf.* **2015**, *120*, 2016–2026. [CrossRef]
24. Gill, H.S.; Singh, T.; Singh, S.; Kim, J.-R.; Caputo, R.; Kaur, G.; Singh, S.; Khosla, A. Active transfer faulting in the NW Sub-Himalaya (India) observed by space-borne topographic analyses. *Quat. Int.* **2021**, *585*, 15–26. [CrossRef]
25. Massonnet, D.; Rossi, M.; Carmona, C.; Adragna, F.; Peltzer, G.; Feigl, K.; Rabaute, T. The displacement field of the Landers earthquake mapped by radar interferometry. *Nature* **1993**, *364*, 138–142. [CrossRef]
26. Bürgmann, R.; Rosen, P.A.; Fielding, E.J. Synthetic Aperture Radar Interferometry to Measure Earth's Surface Topography and Its Deformation. *Annu. Rev. Earth Planet. Sci.* **2000**, *28*, 169–209. [CrossRef]
27. Costantini, M. A novel phase unwrapping method based on network programming. *IEEE Trans. Geosci. Remote Sens.* **1998**, *36*, 813–821. [CrossRef]
28. Costantini, M.; Rosen, P.A. A generalized phase unwrapping approach for sparse data. In Proceedings of the IEEE 1999 International Geoscience and Remote Sensing Symposium. IGARSS'99 (Cat. No.99CH36293), Hamburg, Germany, 28 June–2 July 1999; pp. 267–269. [CrossRef]
29. Monterroso, F.; Bonano, M.; De Luca, C.; Lanari, R.; Manunta, M.; Manzo, M.; Onorato, G.; Zinno, I.; Casu, F. A Global Archive of Coseismic DInSAR Products Obtained Through Unsupervised Sentinel-1 Data Processing. *Remote Sens.* **2020**, *12*, 3189. [CrossRef]
30. Manzo, M.; Ricciardi, G.; Casu, F.; Ventura, G.; Zeni, G.; Borgström, S.; Berardino, P.; Del Gaudio, C.; Lanari, R. Surface deformation analysis in the Ischia Island (Italy) based on spaceborne radar interferometry. *J. Volcanol. Geotherm. Res.* **2006**, *151*, 399–416. [CrossRef]
31. Casu, F.; Manconi, A. Four-dimensional surface evolution of active rifting from spaceborne SAR data. *Geosphere* **2016**, *12*, 697–705. [CrossRef]
32. De Luca, C.; Zinno, I.; Manunta, M.; Lanari, R.; Casu, F. Large areas surface deformation analysis through a cloud computing P-SBAS approach for massive processing of DInSAR time series. *Remote Sens. Environ.* **2017**, *202*, 3–17. [CrossRef]
33. Panchal, H.; Bahuguna, A.; Saraf, A.K.; Das, J. Thermal Anomaly, Co-Seismic Deformation and Seismic Source Pa-rameters Estimation of June 21 2022, Afghanistan Earthquake Employing InSAR Observations. *Pure Appl. Geophys.* **2023**, *180*, 2007–2022. [CrossRef]

34. Qi, Y.; Feng, W.; Zhang, Y.; Wang, D.; Du, Y.; Samsonov, S.V.; Zhang, P.-Z.; Zaray, A.H.; Ansari, A. Fault Geometry, Slip Distribution, and Potential Triggering of the 2022 M w 6.2 Deadly Afghanistan Earthquake Revealed from Geodetic and Weather Data. *Seismol. Res. Lett.* **2023**, *94*, 2154–2166. [CrossRef]
35. Dalal, P.; Senapati, B.; Kundu, B. Co-seismic surface displacement of the June 21, 2022 MW6 Khōst, Afghanistan earthquake from InSAR observations. *Geod. Geodyn.* **2024**, *15*, 201–208. [CrossRef]
36. Wang, R.; Diao, F.; Hoechner, A. SDM-A geodetic inversion code incorporating with layered crust structure and curved fault geometry. *EGU Gen. Assem. Conf. Abstr.* **2013**, *15*, EGU2013-2411-1.
37. Shnizai, Z.; Talebian, M.; Valkanotis, S.; Walker, R. Multiple Factors Make Afghan Communities Vulnerable to Earthquakes. Temblor. 2022. Available online: https://temblor.net/earthquake-insights/multiple-factors-make-afghan-communities-vulnerable-to-earthquakes-14301/ (accessed on 8 August 2024).
38. Wang, H.; Liu, M.; Ye, J.; Cao, J.; Jing, Y. Strain partitioning and stress perturbation around stepovers and bends of strike-slip faults: Numerical results. *Tectonophysics* **2017**, *721*, 211–226. [CrossRef]
39. Cowgill, E.; Yin, A.; Arrowsmith, J.R.; Feng, W.X.; Shuanhong, Z. The Akato Tagh bend along the Altyn Tagh fault, northwest Tibet 1: Smoothing by vertical-axis rotation and the effect of topographic stresses on bend-flanking faults. *GSA Bull.* **2004**, *116*, 1423–1442. [CrossRef]
40. Garvue, M.M.; Spotila, J.A.; Cooke, M.L.; Curtiss, E.R. What Controls Early Restraining Bend Growth? Structural, Morphometric, and Numerical Modeling Analyses From the Eastern California Shear Zone. *Tectonics* **2024**, *43*, e2023TC008148. [CrossRef]
41. Ye, J.; Liu, M.; Wang, H. A numerical study of strike-slip bend formation with application to the Salton Sea pull-apart basin. *Geophys. Res. Lett.* **2015**, *42*, 1368–1374. [CrossRef]
42. Gabrielsen, R.H.; Giannenas, P.A.; Sokoutis, D.; Willingshofer, E.; Hassaan, M.; Faleide, J.I. Analogue experiments on releasing and restraining bends and their application to the study of the Barents Shear Margin. *Solid Earth* **2023**, *14*, 961–983. [CrossRef]
43. Wang, D.; Elliott, J.R.; Zheng, G.; Wright, T.J.; Watson, A.R.; McGrath, J.D. Deciphering interseismic strain accumulation and its termination on the central-eastern Altyn Tagh fault from high-resolution velocity fields. *Earth Planet. Sci. Lett.* **2024**, *644*, 118919. [CrossRef]
44. King, G.; Nábělek, J. Role of Fault Bends in the Initiation and Termination of Earthquake Rupture. *Science* **1985**, *228*, 984–987. [CrossRef]
45. Avouac, J.-P.; Ayoub, F.; Wei, S.; Ampuero, J.-P.; Meng, L.; Leprince, S.; Jolivet, R.; Duputel, Z.; Helmberger, D. The 2013, Mw 7.7 Balochistan earthquake, energetic strike-slip reactivation of a thrust fault. *Earth Planet. Sci. Lett.* **2014**, *391*, 128–134. [CrossRef]